ECS Transactions, 103 (1) 569-580 (2021)
10.1149/10301.0569ecst ©The Electrochemical Society

Modeling of reversible solid oxide cell stacks with an open-source library

Shidong Zhang[a], Roland Peters[a,*], Bob Varghese[a], Robert Deja[a], Nicolas Kruse[a], Steven B. Beale[a,b], Ludger Blum[a], and Ralf Peters[a]

[a]Institute of Energy and Climate Research, IEK-14, Forschungszentrum Jülich, 52425 Jülich, Germany
[b]Mechanical and Materials Engineering, Queen's University, Kingston ON K7L 3N6, Canada
* Corresponding author, Email address: ro.peters@fz-juelich.de

This study describes a homogenized model of reversible solid oxide cell (rSOC) stacks. The model enables steady-state simulations of rSOC stacks in both fuel cell and electrolyzer modes to be conducted. It accounts for multi-component species diffusion, and heat and mass transfer, including thermal radiation and electrochemical reactions. An open-source library, OpenFOAM, provides a platform for the model's implementation. Numerical simulations were performed using an in-house-designed rSOC stack. A previously-developed, one-dimensional Simulink model was also applied to the stack. Both models predict similar output voltages, within 2% difference, under the same operating conditions. Temperature variations were also compared; the stack model's results were closer to experimental measurements than the Simulink model. The new model was able to perform faster simulations (less than 2 hours) for the prescribed stacks.

Introduction

The use of fossil fuels has triggered global climate change. The impacts of this have emerged around the world in the form of climate-related natural disasters (1), reduced agricultural yields (2), and human health effects (3). Various approaches may contribute to the mitigation of this process, including conventional mitigation, negative emissions, and radiative forcing-focused geoengineering (1). The first of these focuses on the reduction of greenhouse gas emissions, whereas the second aims to capture and sequester CO_2 from the atmosphere. The last seeks to stabilize/decrease the global temperature by balancing the Earth's radiative energy budget. The EU has set the goal of achieving net-zero greenhouse gas emissions by the year 2050 (4).

Reversible solid oxide cells (rSOCs) provide a feasible option for reducing greenhouse gas emissions by decreasing the consumption of fossil fuels and increasing the use of clean/renewable energy alternatives. These systems can operate in both fuel cell and electrolysis modes. The former converts chemical energy into electricity, whereas the latter stores electricity in certain fuels, such as hydrogen and/or carbon-monoxide. Given their promising features for future applications, rSOCs have been extensively investigated over the last decade (5,6). Experimental studies have analyzed and prompted the development and improvement of rSOCs and associated stack designs (7–13). Extensive experimental

measurements usually require relatively long time periods, as well as sophisticated equipment. Therefore, numerically-based efforts have been devoted to understanding the operating mechanism and physical details with the aim of rSOC design optimization. A detailed review on the modeling and experimental investigations of SOCs has been published recently (14). A fully-coupled SOC cell model is usually on a multi-scale and must address all or most of the principal processes, which makes it highly complex. From a numerical perspective, the simulations are also computationally-expensive, as the grid density should be high enough to resolve local details, e.g., porous electrodes and gas flow paths, etc. Moreover, an SOC stack normally consists of dozens or hundreds of repeating unit cells.

A detailed, stack-level analysis can be found in the work of Li et al. (15), who conducted simulations using a simplified stack, including 30-unit cells, on a 2-CPU/16-core PC. In a case involving 27 million finite volumes, this took approximately 40 hours. If the energy transfer was omitted, the required hours decreased to 12. To reduce the computation requirements, the porous media approach is commonly applied in order to simplify the stack geometries. Earlier studies were performed by Achenbach (16), Hendriksen (17), Ferguson et al. (18), and Costamagna and Honegger (19). More recent studies are also available (20–24). The basic simplification is achieved by treating the mini-channels as 'porous media', and the resistance due to walls can be expressed as a function of velocities (25), e.g., the hydraulic diameter and friction factor for specific shapes of cross-sections can be easily obtained in laminar flows.

Al-Masri et al. (26) conducted transient simulations to investigate temperature distribution in a short SOFC stack. In this model, each cell was separated into two types of regions, namely, solid and porous. The model was able to predict the temperature distribution and outlet temperature vs. the time with good agreement with the experimental measurements. However, electrochemical reactions were not taken into account. A similar approach was applied by Kvesic et al. (27) to another type of fuel cell stack. Nishida et al. (22–24,28) employed a slightly different method, namely distributed resistance analogy, which was developed by Beale and Zhubrin (25). Similarly, each repeating unit cell consisted of solid and 'porous' regions. However, they were considered in a single layer of mesh, wherein some zones were shared spaces and others were not, e.g., the electrochemically-active zone was a part of all solid/porous regions, but the manifold zones were only parts of the air or fuel's 'porous' region. Heat and mass transfer was specifically considered in the shared spaces (29). With such an approach, the final computational mesh included N layers of grids, where N represents the number of repeating unit cells in a stack. The original work (25) revealed that the simulation results predicted by the stack model was in good agreement with the detailed method. A comparison of the simulation results and experimental data was also conducted (28), and the deviations were not large.

In this study, the model developed by Beale et al. (21–24, 27) is improved upon and implemented within the open-source library, OpenFOAM (30). The solver enables stack-level simulations of both SOFCs and SOECs to be performed. It is then applied to investigate the performance of an rSOC stack, the core part of a 5/15kW-class rSOC system (12). The stack includes four 10-layer sub-stacks and an active cell area per layer of 320 cm^2. It operates in a temperature range of 873–1073 K. The full stack is covered by insulating plates to reduce heat losses to adjacent components and the environment. A 1-D

simulation is also performed using a previously developed Simulink model (31). The following presents the multiple-region technique and the geometric simplification.

Multiple-region approach

The simplification of the detailed geometry is shown in Figure 1. The cross-section displays the important components used to construct a stack. These can be categorized into several regions, namely the interconnect, electrolyte, air, and fuel. Among them, interconnect and electrolytes represent pure solid components, whereas air and fuel include the channels and porous parts of each side (the cathode and anode). In the present model, these regions occupy the same spatial volume, as shown in Figure 1 (b), but with different porosities. The volume fraction can be calculated as the ratio of the regional volume to the total volume.

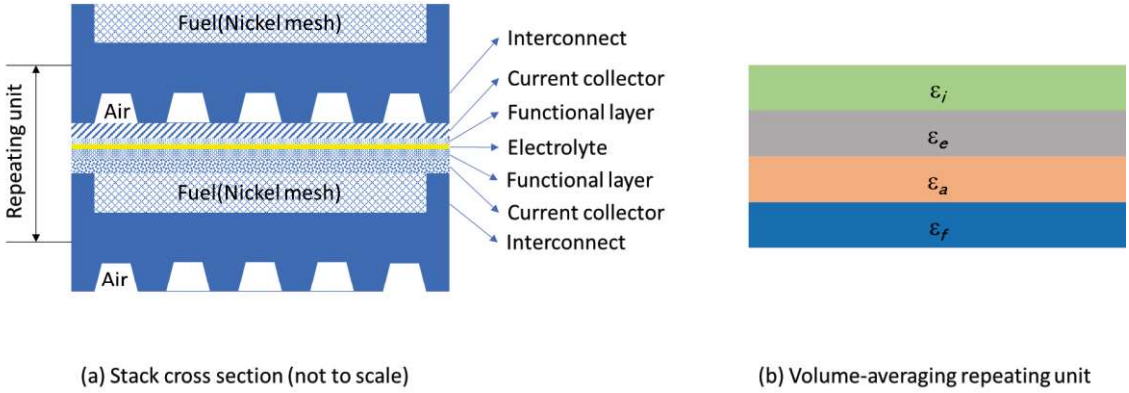

Figure 1. Illustration of geometric simplification in the present model (ε: volume fraction of each region; subscription: *i, e, a, f*: interconnect, electrolyte, air, and fuel).

Geometry

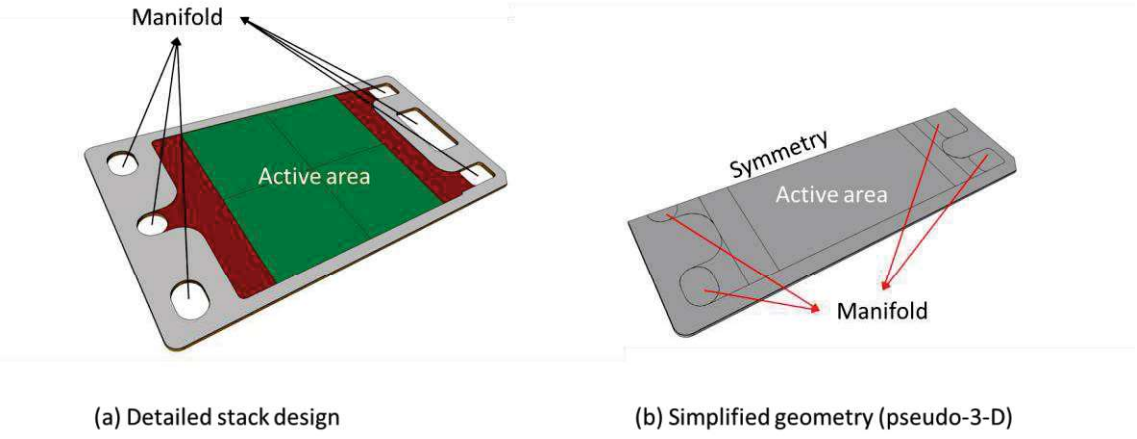

Figure 2. Geometric simplification.

Figure 2 (a) shows the in-plane geometrical information in a repeating unit. The gases are supplied from the left-side manifolds and flow out on the other side. Electrochemical reactions take place in the middle zone, referred to here as the active area, which includes four single-cell zones, each with an active area of $9\times9\,\mathrm{cm}^2$. The design is symmetrical; therefore, this study considers a half-stack in its numerical simulations. By applying the

multiple-region approach presented in the last section (see Figure 1), the detailed geometry can be further simplified, as shown in Figure 2 (b).

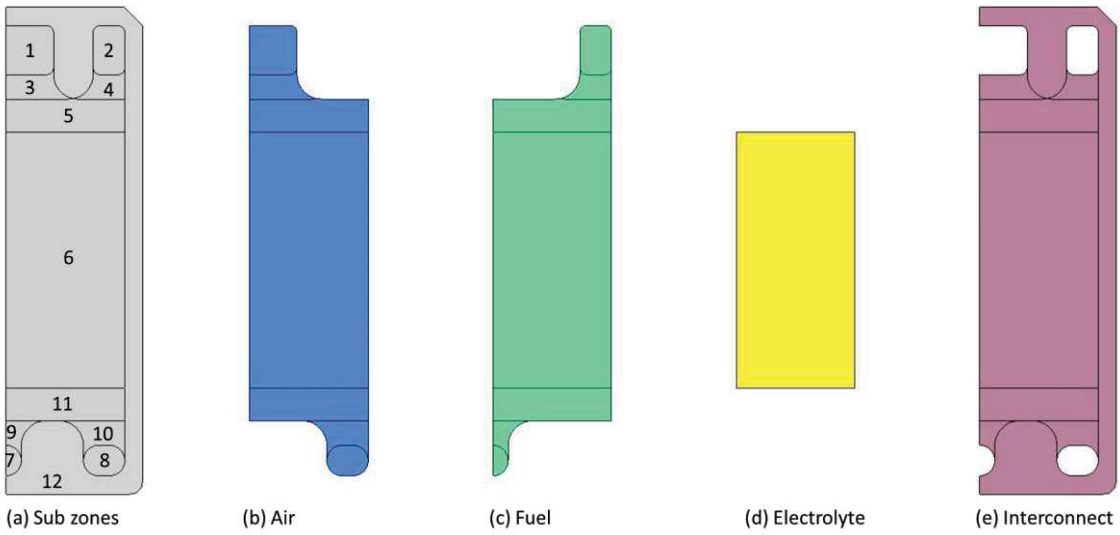

Figure 3. The sub-regions modeled in the present study. (Manifold zones: 1, 2, 7, and 8; connection zones: 3, 4, 9, and 10; transition zones: 5 and 11; core zone: 6)

Figure 3 presents an in-plane cross-section of the simplified geometry. The surface consists of 12 sub-zones, classified as manifold zones, connection zones, transition zones, and a core zone. Among them, manifold zones are pure fluid, whereas zone 12 is pure solid. The sub-regions can be constructed by recombining some of these.

Computational domain

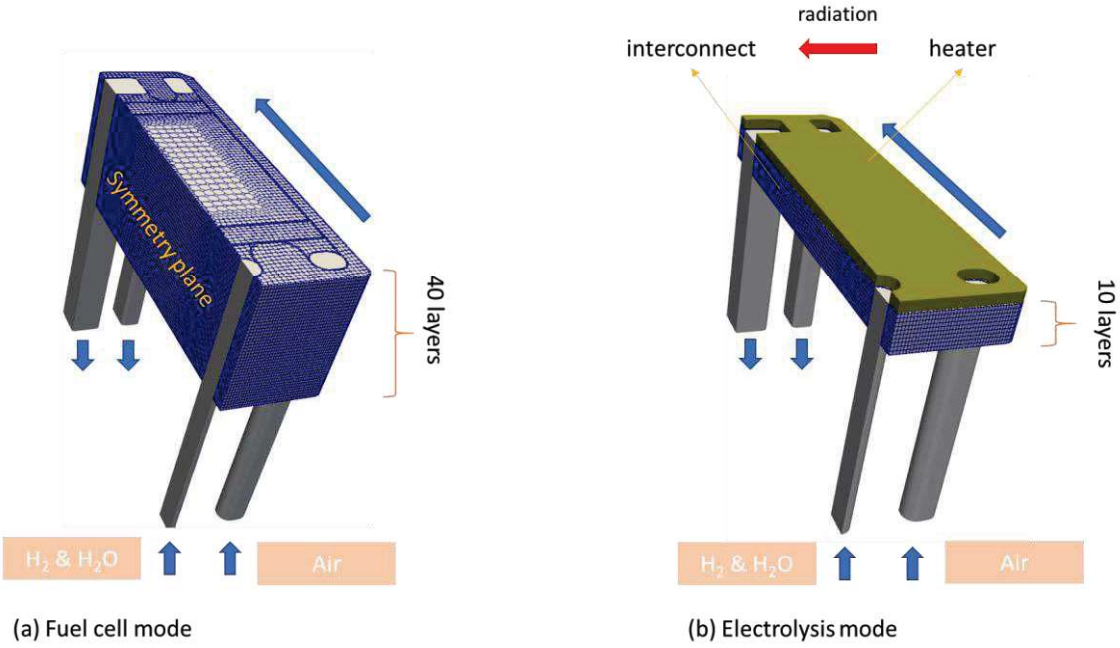

Figure 4. Computational domain.

The detailed assembly of the rSOC stack discussed here can be found in the work of Peters et al. (12). The simplified geometry was tessellated using a computational mesh

constructed with cfMesh cf-mesh (32), which was applied to the ground surfaces and then extruded in the normal direction to create the computational mesh for the entire stack. Figure 4shows the computational domains for the stack in fuel cell and electrolysis modes, respectively. In fuel cell mode, sufficient air is supplied from the manifold to cool the stack's temperature due to the exothermic electrochemical reaction. In this case, the whole stack, with 40 repeating unit cells, is taken into account. In electrolysis mode, the endothermic electrochemical reaction occurs if the stack operates below the thermoneutral voltage; therefore, a heating plate is placed between every two sub-stacks. A 10-layer sub-stack with a symmetry plane on the lower stack surface and heating plate on the top are also modeled.

Numerical model

The model considers the major physical processes in rSOC stacks by means of a volume-averaging method. These processes include thermal-fluid interactions, thermal radiation, and electrochemical reactions. The governing equations are discretized and solved in a finite volume domain/mesh using an open-source CFD library, namely OpenFOAM. A detailed description of the model can be found in several previous works (21, 23, 24, and 27). A brief introduction is also provided below.

Assumptions:

1. The simulations are steady state.
2. The gases are laminar flow regimes, incompressible, and ideal.
3. Fick's law is used for multi-component species transfer.
4. Ohmic resistance only exists in the electrolyte with an area-specific-resistance.
5. Thermal/mechanical deformation is not considered.
6. Internal thermal radiation is negligible.
7. Heat losses are constant on the outer surfaces.

Governing equations

The equations solved in this study consist of continuity, momentum, species transfer, and enthalpy factors. Among them, the enthalpy equation applies to both the fluid and solid regions, whereas the remaining equations apply to the fluid regions in terms of air and fuel.

The generic form of the governing equations is written as:

$$\underbrace{\nabla\cdot\left(\rho\mathbf{u}\varphi\right)}_{\text{convection}}=\underbrace{\nabla\cdot\left(\Gamma\nabla\varphi\right)}_{\text{diffusion}}+\underbrace{\sum_{j}\alpha_{j}\left(\varphi-\varphi_{j}\right)}_{\text{inter-phase}}+\underbrace{S}_{\text{source}} \tag{1}$$

where φ means the general variables (scalar/vector), ρ (kg m^{-3}) represents the density, $\mathbf{u}$ (m s^{-1}) the velocity, Γ the coefficient for diffusion, α denotes the inter-phase transfer coefficient, and S gives the source/sink terms, for example, due to electrochemical reactions. The four terms represent the convection, diffusion, inter-phase, and source terms. The convection term is only valid in the fluid regions. The inter-phase term considers the (heat) transfer between adjacent regions.

The entailed governing equations in the fluid regions are shown as follows:

$$\nabla \cdot \left(\varepsilon \rho \mathbf{u} \right) = \varepsilon \dot{m}''' \tag{2}$$

$$\nabla \cdot \left(\varepsilon \rho \mathbf{u}\mathbf{u} \right) = -\varepsilon \nabla p + \nabla \cdot \left(\varepsilon \mu \nabla \mathbf{u} \right) + \varepsilon \mathbf{F}_D \tag{3}$$

$$\nabla \cdot \left(\varepsilon \rho \mathbf{u} y_{\mathrm{k}} \right) = \nabla \cdot \left(\varepsilon \Gamma^{\mathrm{eff}} \nabla y_{\mathrm{k}} \right) + \varepsilon \dot{m}_{\mathrm{k}}''' \tag{4}$$

$$\nabla \cdot \left(\varepsilon \rho \mathbf{u} h \right) = \nabla \cdot \left(\varepsilon \lambda^{\mathrm{eff}} \nabla h + \varepsilon \dot{q}''_{\mathrm{rad}} \right) + \varepsilon \sum_{\mathrm{j}} \alpha_{\mathrm{j}} \left(T - T_{\mathrm{j}} \right) \tag{5}$$

where ε denotes the volume fraction of the region, $\mathbf{u}$ (m s^{-1}) is the interstitial velocity, $\dot{m}'''$ (kg m^{-3} s^{-1}) represents the mass source/sink due to the electrochemical reaction, p (Pa) is the pressure, μ (Pa s) the dynamic viscosity, y represents the mass fraction of each species, Γ^{eff} (kg m^{-2} s^{-1}) denotes the effective diffusion coefficient, h (J m^{-3}) the enthalpy, λ (m^2 s^{-1}) means thermal diffusivity, T (K) represents the temperature, $\dot{q}''_{\mathrm{rad}}$ (J m^{-2} s^{-1}) is the radiative heat flux, and $\mathbf{F}_D$ (N m^{-3}) the drag force due to the wall fractions. The calculation of interphase coefficient, α (J K^{-1} s^{-1}), and drag force, $\mathbf{F}_D$, can be found in previous work (21, 24, 27).

The governing equation solved in the solid region yields:

$$\nabla \cdot \left(\varepsilon \lambda^{\mathrm{eff}} \nabla h + \varepsilon \dot{q}''_{\mathrm{rad}} \right) + \varepsilon \sum_{j} \alpha_j \left(T - T_j \right) + \varepsilon \dot{q}''' = 0 \tag{6}$$

where $\dot{q}'''$ (J m^{-3} s^{-1}) is the heat source/sink from the joule and electrochemical heat.

Electrochemical reaction: The cell voltage, V_{cell}, is related to the local current density by means of the Kirchhoff-Ohm relationship:

$$V_{cell} = E - Ri'' \tag{7}$$

where E (V) is the Nernst potential, R (Ω m^2) the area specific resistance (ASR), and i'' (A m^{-2}) denotes the current density. The formulation to calculate the ASR employed here is (8):

$$R = A_0 \exp\left(-\frac{\mathrm{R}_g T}{E_a} \right) \tag{8}$$

where A_0 (Ω m^2) is the coefficient, E_a (J mol^{-1}) represents the active energy, and R_g (J mol^{-1} K^{-1}) means the universal gas constant.

The mass and heat source/sink terms are calculated as:

$$\dot{m}_{\mathrm{k}}''' = \mathrm{sgn}\left(\mathrm{k} \right) \frac{M_{\mathrm{k}} i'''}{nFH_{\mathrm{cell}}} \tag{9}$$

$$\dot{m}''' = \sum_{j} \dot{m}_j''' \tag{10}$$

$$\dot{q}''' = \left(\frac{-\Delta S \cdot T}{F} + Ri'' \right) \frac{i''}{H_{\text{cell}}} \tag{11}$$

where the $\text{sgn}(\text{k})$ is a sign factor of species k, +: products and -: reactants, n is the number of electron transfers during the reaction, H_{cell} (m) denotes the thickness of the repeating unit cell, F (C mol^{-1}) represents Faraday's constant, and S (J mol^{-1} K^{-1}) stands for the entropy.

Thermal radiation: For rSOC stacks to achieve their high operating temperatures, thermal radiation cannot be neglected. In this study, it helps maintain the stack temperature in electrolysis mode by transferring it from an external heater to the stack interconnects. A viewFactor model, also called a surface-to-surface model (33), is employed by assuming all walls to be gray and diffuse.

The radiation energy is calculated with:

$$\mathbf{E} = \mathbf{KJ} = (\mathbf{I} - \rho\mathbf{F})\mathbf{J} \tag{12}$$

where $\mathbf{I}$ is an identity matrix, ρ is the reflectivity, equal to $1-\varepsilon$ (emissivity), $\mathbf{F}$ represents the view factor matrix, and $\mathbf{J}$ the radiosity matrix.

Results

This model was applied to the in-house-designed rSOC stack, which was operated in both fuel cell and electrolysis modes. The operating conditions are displayed in TABLE I. Detailed information on the stack assembly and component properties can be found in previously published works (e.g., 11, 12, 22, and 33). All of the numerical simulations were conducted serially on a Linux machine with an Intel® Core™ i7-9700 K CPU @ 3.60 GHz, and 32 GB of RAM. Each case required less than 2 hours.

TABLE I. Operating conditions.

		SOFC		SOEC	Unit
Pressure	Air	101325	Air	101325	Pa
	Fuel	101325	Fuel	101325	
Temperature	Air	848	Air	978	K
	Fuel	848	Fuel	978	
Inlet flux	Air	0.31	Air	0.00027	mol s^{-1}
	Fuel	0.047/H_2 0.0038/H_2O	Fuel	0.0055/H_2 0.012/H_2O	
Utilization	Air	25.4 %		--	--
	Fuel	70.0 %			
Heat loss		300		34.1	W
Heating power		0		249.6	W
Current		80		-81	A

Fuel cell mode

In the present case, the stack operates with a mean current density of 0.49 A cm^{-2}. The output voltages are experimentally-measured and numerically predicted as 0.818 V, 0.821 V, and 0.824 V, for the experiment, Simulink, and the present stack model, respectively. Figure 5 displays a comparison of the local temperature variations. The white line in Figure 6 marks the locations of the measurements. It can be seen that both numerical methods predict temperature variations very close to the data points measured experimentally. The local temperatures remain nearly constant near the inlet and outlet manifolds. In the middle zone, the temperature increases due to the exothermic reaction and Joule heating. From the inlet to the outlet, the maximum temperature difference is approximately 200 K.

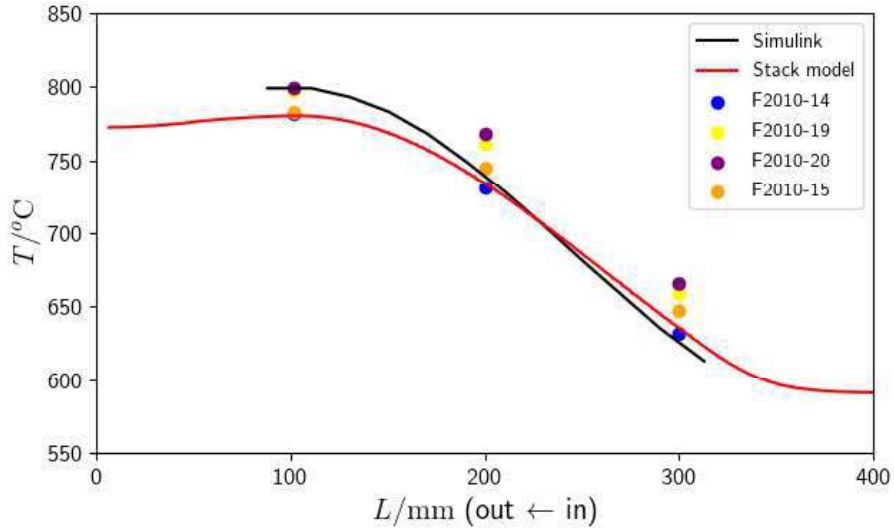

Figure 5. A comparison of temperature variations from the inlet to the outlet. $\bar{i} = 0.49\ \mathrm{A\,cm^{-2}}$ in fuel cell mode.

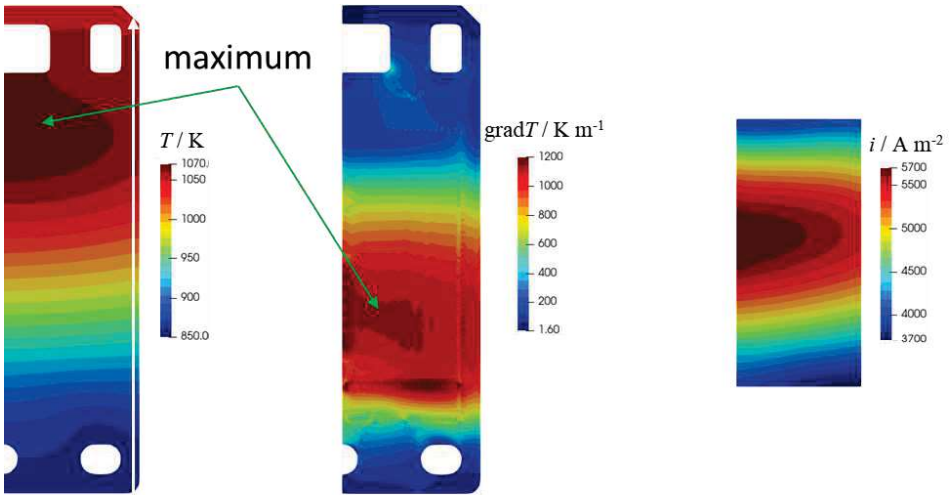

Figure 6. Distributions of the temperature (left), temperature gradient (middle), and current density (right) in fuel cell mode.

Figure 6 presents the temperature, temperature gradient, and current density distributions for a cross-section located at one quarter of the height in the normal direction. The maximum temperature is located near the outlet manifold, at a value of 1070 K. The maximum temperature gradient is found in the core (active) zone. Attention should be paid to the materials to ensure the integrity and performance of the operating stack. The current density distribution is also shown, which increases at first and then decreases. With the increase in temperature, the ASR value decreases; meanwhile, the reactant concentrations decrease and the product concentration increases; therefore, the maximum local current density appears in the middle areas. The current density varies in the range of 0.2 A cm^{-2}.

Electrolysis mode

In this case, the mean current density is fixed at -0.5 A cm^{-2}. The experimental, stack model, and Simulink model results, in terms of cell voltages, yield 1.240 V, 1.234 V, and 1.260 V, respectively. Additional heat is, therefore, supplied by a heating plate to the stack interconnects in the form of radiation. Figure 7 displays the local temperature variations for the experimental and numerical results on the line marked in Figure 8. It can be observed that the present stack model exhibits better agreement with the experimental data, while deviations are observed between the Simulink model and other methods. The temperature variation near the outlet manifold remains nearly constant, which is similar to the fuel cell case. In other zones, the temperature increases monotonically.

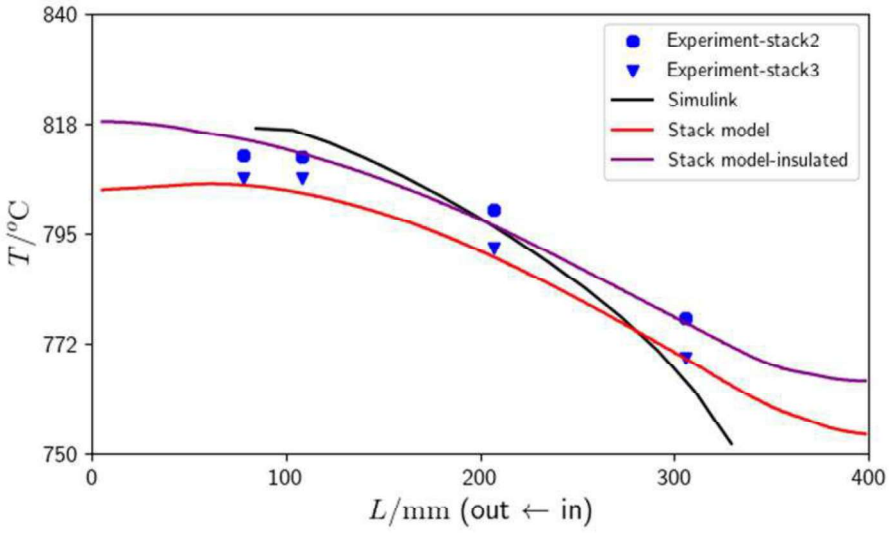

Figure 7. Comparison of the temperature variations from the inlet to the outlet. $\bar{i} = -0.5\ \mathrm{A\,cm^{-2}}$ in electrolysis mode.

The temperature distribution is shown in Figure 8, which also presents the temperature gradient and current density distribution. The maximum temperature appears near the outlet manifold, whereas the maximum temperature gradient is found close to the inlet manifold. The maximum current density (magnitude) is located in the middle of activate area, but closer to the inlet side. The current density varies in the range of 0.075 A cm^{-2}. Furthermore, the overall temperature and current density distributions are more uniform compared to the fuel cell case.

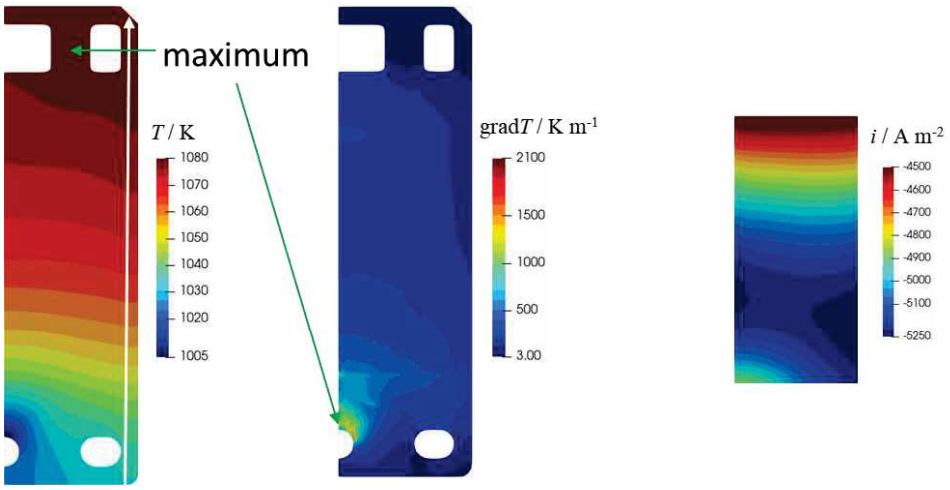

Figure 8. Distributions of temperature (left), temperature gradient (middle), and current density (right) in electrolysis mode.

Conclusions

In this study, a 3-D, steady-state, homogenized, CFD model was developed for rSOC stack simulations. It incorporates thermal and fluid flow, electrochemical reactions, and thermal radiation. A multiple-region approach was used to address the physical processes in different regions, including fluids and solids. The model was then applied to an in-house-designed rSOC stack.

The 3-D model presents voltages and local temperature variations close to both experimentally-measured values, and to the results of the Simulink model's predictions in both fuel cell and electrolysis modes. The 3-D model outperforms the Simulink model in its prediction of local temperatures.

In all operating modes, the temperature increases in magnitude from the inlet to the outlet manifolds and the maximum temperatures appear near the latter. The maximum temperature gradients can be found in the activate area and fuel inlet manifold for fuel cell and electrolysis cases, respectively. These results must be given special consideration when optimizing stack geometry.

The maximum current densities for both modes are located in the middle of the activation area. However, the distribution is more uniform in electrolysis mode than in the fuel cell case.

Acknowledgements

The authors appreciate the help from colleagues at the Forschungszentrum Jülich GmbH, who aided in realizing the system, and to the Helmholtz Society for financing these activities. The language review and editing performed by Mr. Christopher Wood is also appreciated.

References

1. S. Fawzy, A. I. Osman, J. Doran, and D. W. Rooney, *Environ Chem Lett*, **18**, 2069–2094 (2020).

2. G. S. Malhi, M. Kaur, and P. Kaushik, *Sustainability*, **13**, 1318 (2021).

3. P. Cianconi, S. Betrò, and L. Janiri, *Front Psychiatry*, **11** (2020).

4. Anonymous, *Climate Action - European Commission* (2016) https://ec.europa.eu/clima/policies/strategies/2050_en.

5. X. Zhang et al., *Journal of Power Sources*, **195**, 685–702 (2010).

6. Z. Li, H. Zhang, H. Xu, and J. Xuan, *Renewable and Sustainable Energy Reviews*, **141**, 110863 (2021).

7. L. Blum et al., *ECS Transactions*, **57**, 23–33 (2013).

8. R. Peters et al., *Journal of Power Sources*, **328**, 105–113 (2016).

9. Y. Yan, Q. Fang, L. Blum, and W. Lehnert, *Electrochimica Acta*, **258**, 1254–1261 (2017).

10. Q. Fang, L. Blum, and D. Stolten, *J. Electrochem. Soc.*, **166**, F1320 (2019).

11. Q. Fang et al., *J. Electrochem. Soc.*, **167**, 144508 (2020).

12. R. Peters et al., *J. Electrochem. Soc.* (2021).

13. H. Aslannejad, L. Barelli, A. Babaie, and S. Bozorgmehri, *Applied Energy*, **177**, 179–186 (2016).

14. S. B. Beale et al., *Progress in Energy and Combustion Science*, **85**, 100902 (2021).

15. A. Li, C. Song, and Z. Lin, *Applied Energy*, **190**, 1234–1244 (2017).

16. E. Achenbach, *Journal of Power Sources*, **49**, 333–348 (1994).

17. P. V. Hendriksen, *ECS Proceedings Volumes*, **1997–40**, 1319–1328 (1997).

18. J. R. Ferguson, J. M. Fiard, and R. Herbin, *Journal of Power Sources*, **58**, 109–122 (1996).

19. P. Costamagna and K. Honegger, *Journal of The Electrochemical Society*, **145**, 3995–4007 (1998).

20. M. Navasa et al., *International Journal of Hydrogen Energy*, **43**, 11913–11931 (2018).

21. M. Navasa, X.-Y. Miao, and H. L. Frandsen, *International Journal of Hydrogen Energy*, **44**, 23330–23347 (2019).

22. R. T. Nishida, S. B. Beale, and J. G. Pharoah, *Int. J. Hydrogen Energy*, **41**, 20592–20605 (2016).

23. R. T. Nishida, S. B. Beale, J. G. Pharoah, L. G. J. de Haart, and L. Blum, *Journal of Power Sources*, **373**, 203–210 (2018).

24. S. B. Beale et al., *Heat and Mass Transfer in Fuel Cells and Stacks*, "50 Years of CFD in Engineering Sciences," A Commemorative Volume in Honour of D. Brian Spalding., Springer, (2019).

25. S. B. Beale and S. V. Zhubrin, *Numerical Heat Transfer, Part B: Fundamentals*, **47**, 573–591 (2005).

26. A. Al-Masri, M. Peksen, L. Blum, and D. Stolten, *Applied Energy*, **135**, 539–547 (2014).

27. M. Kvesić et al., *International Journal of Hydrogen Energy*, **37**, 2430–2439 (2012).

28. S. Zhang et al., *ECS Transactions*, **86**, 287–300 (2018).

29. S. B. Beale, Y. Lin, S. V. Zhubrin, and W. Dong, *Journal of Power Sources*, **118**, 79–85 (2003).

30. OpenCFD, http://www.openfoam.com.

31. M. Engelbracht, R. Peters, L. Blum, and D. Stolten, *J. Electrochem. Soc.*, **162**, F982 (2015).

32. *Creative Fields* https://cfmesh.com/.

33. J. R. Howell, M. P. Menguc, and R. Siegel, *Thermal radiation heat transfer*, CRC press, (2010).

34. M. Peksen, *International Journal of Hydrogen Energy*, **40**, 12362–12369 (2015).